Exploring NGC 2345: A Comprehensive Study of a Young Open Cluster through Photometric and Kinematic Analysis

Kuldeep Belwal[1], D. Bisht[1] , Mohit Singh Bisht[1], Geeta Rangwal[2] , Ashish Raj[1] , Arvind K. Dattatrey[3] ,
R. K. S. Yadav[3], and B. C. Bhatt[4]
[1] Indian Centre for Space Physics, 466 Barakhola, Singabari Road, Netai Nagar, Kolkata 700099, India
[2] South-Western Institute for Astronomy Research, Yunnan University, Kunming 650500, People's Republic of China
[3] Aryabhatta Research Institute of Observational Sciences, Manora Peak, Nainital 263129, India
[4] Indian Institute of Astrophysics, 560034 Bangalore, India

Abstract

We conducted a photometric and kinematic analysis of the young open cluster NGC 2345 using CCD *UBV* data from 2 m Himalayan Chandra Telescope, Gaia Data Release 3, Two Micron All-Sky Survey, and the Photometric All-Sky Survey data sets. We found 1732 most probable cluster members with membership probability higher than 70%. The fundamental and structural parameters of the cluster are determined based on the cluster members. The mean proper motion of the cluster is estimated to be $\mu_\alpha \cos \delta = -1.34 \pm 0.20$ and $\mu_\delta = 1.35 \pm 0.21$ mas yr^{-1}. Based on the radial density profile, the estimated radius is $\sim 12\farcm8$ (10.37 pc). Using color–color and color–magnitude diagrams, we estimate the reddening, age, and distance to be 0.63 ± 0.04 mag, 63 ± 8 Myr, and 2.78 ± 0.78 kpc, respectively. The mass function slope for main-sequence stars is determined as 1.2 ± 0.1. The mass function slope in the core, halo, and overall region indicates a possible hint of mass segregation. The cluster's dynamical relaxation time is 177.6 Myr, meaning ongoing mass segregation, with complete equilibrium expected in 100–110 Myr. Apex coordinates are determined as $-40\fdg89 \pm 0.12$, $-44\fdg99 \pm 0.15$. The cluster's orbit in the Galaxy suggests early dissociation into field stars due to its close proximity to the Galactic disk.

Unified Astronomy Thesaurus concepts: Open star clusters (1160); Orbits (1184); Initial mass function (796); Interstellar extinction (841)

1. Introduction

A star cluster comprises a collection of stars, providing a natural laboratory-like setting to develop theoretical models and apply them to gain insights into stellar evolution. Open clusters (OCs) are gatherings of stars originating from the same molecular cloud, characterized by the same age, chemical composition, and distance; however, stars' luminosity and masses are different (Yontan 2023). Typically composed of a few tens to several thousand stars, they loosely aggregate and remain gravitationally bound to each other. In our Galaxy, most, if not all, stars are born in clusters (Portegies Zwart et al. 2010). The study of star clusters is crucial to understand star formation and stellar evolution. OCs are relatively young systems, witnessing recent star formation events, and are predominantly located in the spiral arms of the Milky Way. Young open clusters are typically situated within the densely populated environment of the Galactic disk. Therefore, it is essential to differentiate cluster members from field stars to estimate their physical parameters accurately (Carraro et al. 2008; Dias et al. 2018). Numerous recent studies have conducted membership analyses of stars in the vicinity of open clusters and have explored various cluster properties (Cantat-Gaudin et al. 2018; Castro-Ginard et al. 2018, 2019; Bisht et al. 2019, 2020; Liu & Pang 2019). The release of Gaia Data Release 2 (DR2) data in 2018 marked a revolution in astronomy, providing unprecedented levels of accuracy in astrometry data (Cantat-Gaudin et al. 2019; Monteiro &

Dias 2019). Membership helps to study the distribution of luminosity and mass during star formation, which is known as the initial mass function (IMF; Maurya et al. 2020). Whether the IMF is universal in time and space or depends on various star-forming conditions remains a subject of debate (Bastian et al. 2010; Dib & Basu 2018).

The young open clusters are essential tools to study the effect of mass segregation, where massive stars are concentrated toward the center and lower-mass stars spread in the outer region. Whether mass segregation in star clusters is primarily due to the dynamical evolution of the cluster or the star formation process itself is a subject of ongoing research and debate in astrophysics (Dib et al. 2018).

The young open cluster NGC 2345 (C0706−130) is located in the constellation of Canis Major ($\alpha_{2000} = 07^h08^m18^s$, $\delta_{2000} = -13°11'36''$) and corresponding Galactic coordinates ($l = 226°.58$, $b = -2°.31$) given in the WEBDA open cluster data set.[5] The cluster identification chart is taken from the Digitized Sky Survey (DSS) and shown in Figure 1.[6] The estimated distance, reddening ($E(B - V)$), and age of this cluster fall within the ranges of 2.2–3.0 kpc, 0.59–0.68 mag, and 55–79 Myr (Kharchenko et al. 2005, 2013; Carraro et al. 2014; Cantat-Gaudin et al. 2018; Alonso-Santiago et al. 2019; Singh et al. 2022). Kharchenko et al. (2005) derived the core and cluster radius as $4\farcm2$ and $7\farcm2$, respectively, whereas Alonso-Santiago et al. (2019) estimated the core radius $3\farcm44 \pm 0\farcm08$, tidal radius $18\farcm7 \pm 1\farcm2$, and metallicity [Fe/H] = −0.28 for the cluster. In various past studies, a non-radial distribution of dust associated with the cluster was observed, with variable

---

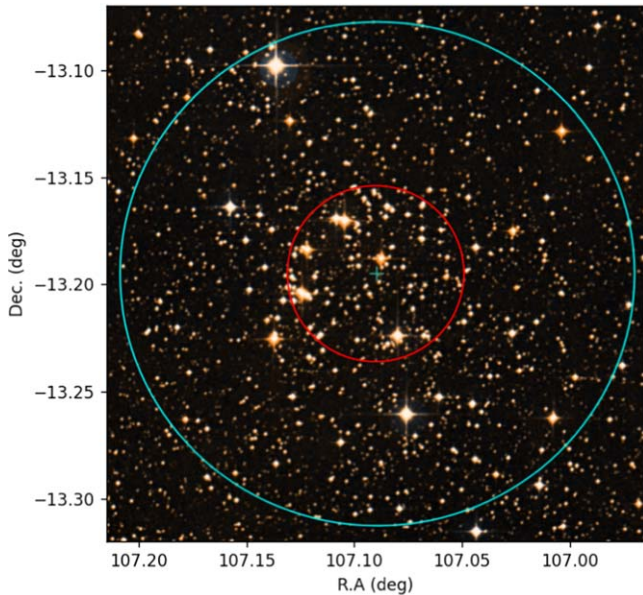[5] https://webda.physics.muni.cz/
[6] https://simbad.u-strasbg.fr/simbad/

Figure 1. Identification chart of NGC 2345 of size 15×15 arcmin^2 taken from the DSS and oriented in the northeast direction (north is up and east is left). The inner circle represents the core radius ($3\rlap{.}'9$), while the outer ring denotes the cluster radius ($12\rlap{.}'8$).

Table 1
Log of Observations, with Dates, Exposure Times, and Air Masses for each Passband

Cluster/Standard Field	Filters	Exp. (s) × No. of Frames	Airmass
NGC 2345	V	50 × 2	1.61–1.66
		30 × 3	
	B	100 × 3	1.56–1.58
	U	180 × 3	1.51–1.53
PG 1525	V	80 × 5	1.30–1.52
	B	150 × 6	1.32–1.59
	U	300 × 6	1.31–1.61

Note. Data were taken on 2004 February 2/3.

reddening ($E(B - V)$) ranging from 0.4 to 1.2 mag (Moffat 1974; Carraro et al. 2014; Alonso-Santiago et al. 2019). We used the radial velocity $58.41 \pm 0.15 \text{ km s}^{-1}$ provided by Dias et al. (2021) and Carrera et al. (2022) in the further analysis.

Previous studies of cluster NGC 2345 have shown a range in the fundamental parameters. However, these parameters were not determined using the cluster members. Thanks to the Gaia Data Release 3 (DR3) survey, we now have access to the much more precise proper motions of the stars in this cluster. These proper motions have been used to calculate the membership probability, which helps us identify the members of the clusters. For the first time, we analyzed the cluster members to determine the fundamental parameters of cluster NGC 2345. This cluster presents a valuable opportunity to study stellar evolution as it contains blue and red supergiants, has a low metallicity, and has a high fraction of Be stars (Alonso-Santiago et al. 2019). However, further detailed analysis is needed due to the peculiarity of this cluster and the lack of studies on its members.

Estimating the orbital parameters of the young open cluster NGC 2345 is pivotal for unraveling its historical and future trajectory within the Milky Way. We gain insights into the underlying Galactic dynamics and gravitational forces influencing this object by determining the cluster's orbit shape, orientation, and velocity. This information contributes to the understanding of the cluster's formation and evolutionary history and sheds light on its interactions with other structures in the Milky Way and the conditions prevalent during its birth. The derived orbital parameters serve as a crucial benchmark for meticulous comparisons with theoretical models, refining our understanding of Galactic dynamics and extending our more comprehensive knowledge of the evolutionary processes governing young open clusters in our Galaxy.

This analysis presents a photometric study for the open cluster NGC 2345. We investigated the spatial structure, fundamental parameters, extent, reddening, and age of the cluster, aiming to gain insights into its dynamical evolution. This analysis is based on kinematic and CCD photometric data extending to approximately $V = 19$ mag. We estimated membership probabilities for stars within the NGC 2345 cluster down to $G \sim 20$ mag. We used high-probability members to analyze the mass function and mass segregation. The paper is structured as follows. Section 2 presents the observations and data analysis. Section 3 discusses the stellar membership within the clusters. In Section 4, we derive the structural parameters of the clusters, followed by the estimation of physical parameters in Section 6. Section 7 explores the dynamical evolution of the clusters. Finally, our work is summarized in Section 8.

2. Observations and Data Reduction

The photometric observations for this cluster were conducted using the 2.0 m Himalayan Chandra Telescope (HCT) at Hanle, operated by the Indian Institute of Astrophysics, Bangalore, India. The Hanle Faint Object Spectrograph Camera (HFOSC), which is an imager cum spectrograph, was used for photometric observation of NGC 2345 in *UBV* Bessel filters. The detector is a $2\text{k} \times 4\text{k}$ CCD, where the central $2\text{k} \times 2\text{k}$ pixels were used for imaging. The pixel size is 15 μm with an image scale of $0\rlap{.}''297 \text{ pixel}^{-1}$. The field of view for imaging is approximately 10×10 arcmin^2, readout noise 4.8 e^-, and gain 1.22 e^- per ADU. The observations have a typical mean signal-to-noise ratio (S/N) of >1000. The observing log is given in Table 1. We observed many bias and twilight flat-field frames in the *UBV* filters and multiple short- and long-exposure frames of the target and standard fields at night. Standard field PG 1525 of Landolt (1992) was observed to calibrate the photometry of cluster stars. To perform the initial processing of the raw data, we utilized the IRAF[7] data reduction packages, which include bias subtraction, flat-fielding, and cosmic-ray removal. The instrumental magnitudes were estimated through point-spread function (PSF) fitting using the DAOPHOT II (Stetson 1987; Worrall et al. 1992) package.

2.1. Photometric Calibration

We also observed the standard field PG 1525 (Landolt 1992) during the same observing night for photometric calibration. The five standard stars (PG 1525-071, 071A, 071B, 071C, 071D) used in the calibration have brightness and color ranges $9 \leqslant V \leqslant 19$ and $0.3 \leqslant B - V \leqslant 2.0$ respectively. For the

---

[7] The Image Reduction and Analysis Facility (IRAF) is distributed by the National Optical Astronomy Observatories (NOAO).

Table 2
Derived Standardization Coefficients and Errors

Filters	Color Coeff(C)	Zero-points(Z)
V	-0.001 ± 0.045	0.75 ± 0.04
B	0.105 ± 0.039	1.18 ± 0.03
U	-0.166 ± 0.017	3.51 ± 0.01

extinction coefficients, we assumed the typical values for the Hanle observing site (Stalin et al. 2008). For translating the instrumental magnitude to the standard magnitude, the calibration equations using the least-squares linear regression are as follows:

$$v = V + Z_V + C_V(B - V) + k_V X \qquad (1)$$

$$b = B + Z_B + C_B(B - V) + k_B X \qquad (2)$$

$$u = U + Z_U + C_U(U - B) + k_U X. \qquad (3)$$

Here, u, b, v denote the instrumental magnitudes, U, B, V are the standard magnitudes, X is airmass, and k_i are the extinction coefficients. The calculated color coefficients (C) and zero-points (Z) for different filters are listed in Table 2. The error in color coefficients and zero-points are 0.01–0.04 mag. The internal errors in each filter derived from DAOPHOT are plotted against V magnitude in Figure 2. This figure shows that the average photometric error is $\leqslant 0.15$ mag for the B and V filters at $V \sim 19$ mag, and it is $\leqslant 0.2$ mag for the U filter at $V \sim 19$ mag. Specifically, the error amount for the V filter is 0.08 mag at 16 and 0.1 mag at 19 mag.

We converted the CCD X and Y pixel position of stars into R.A. and decl. (J2000) using the CCMAP and CCTRAN tasks provided in IRAF. The resulting R.A. and decl. values have standard deviations of $\sim 0\rlap{.}''1$.

We plotted the color–magnitude and color–color diagram, as shown in Figure 3, using 426 stars from the HCT observation. This figure shows the contamination of field stars that needs to be removed from our sample to estimate parameters precisely.

2.2. Archived Data

2.2.1. Gaia DR3

Gaia DR3 (Vallenari et al. 2023) is used for the astrometric study of NGC 2345 and determined structural parameters of the cluster. Gaia DR3 provided celestial positions and G-band magnitudes for a vast data set of around 1.8 billion sources, with a magnitude measurement extending up to 21 mag. Additionally, Gaia DR3 provides valuable parallax, proper-motion, and color information ($G_{BP} - G_{RP}$) for a subset of this data set, specifically 1.5 billion sources. The uncertainties in parallax values are ~ 0.02–0.03 mas for sources at $G \leqslant 15$ mag and ~ 0.07 mas for sources with $G \sim 17$ mag. We collected data for NGC 2345 within a 25′ radius, considering the previously estimated cluster core and tidal radii of 3′.44 and 18′.7, respectively, by Alonso-Santiago et al. (2019). The cluster's proper motions and corresponding errors are graphically represented against G magnitude in Figure 4. The uncertainties in the corresponding proper-motion components are ~ 0.01–0.02 mas yr^{-1} (for $G \leqslant 15$ mag), ~ 0.05 mas yr^{-1} (for $G \sim 17$ mag), ~ 0.4 mas yr^{-1} (for $G \sim 20$ mag), and ~ 1.4 mas yr^{-1} (for $G \sim 21$ mag).
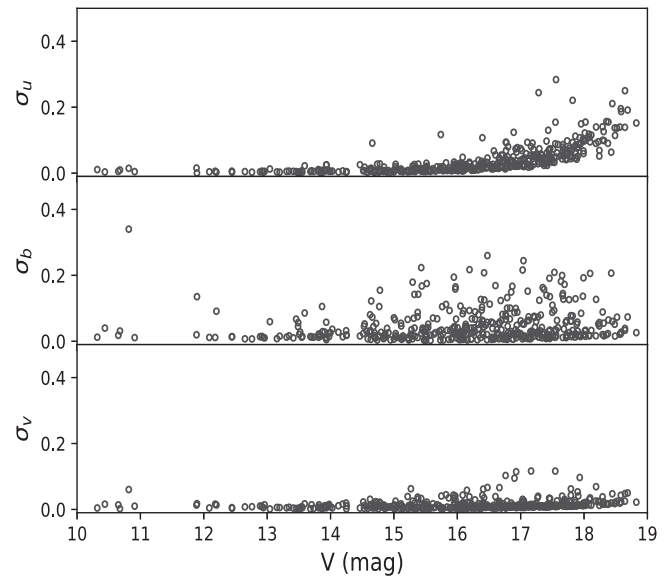

Figure 2. Photometric errors in different filters against V magnitude.

2.2.2. 2MASS

This study used Two Micron All-Sky Survey (2MASS) data for the cluster NGC 2345. This data set has been collected via the two highly automated 1.3 m telescopes, one at Mt. Hopkins, Arizona, USA, and the other at CTIO, Chile, with three 3 channel cameras (256×256 array of HgCdTe detectors). The 2MASS database comprises photometric data in the near-infrared J, H, and K bands, reaching limiting magnitudes of 15.8, 15.1, and 14.3, respectively. These data are available with an S/N greater than 10. We performed a cross-match of our data set with 2MASS data using the Topcat software.[8]

2.2.3. APASS

The American Association of Variable Star Observers (AAVSO) Photometric All-Sky Survey (APASS) is organized in five filters: B, V (Landolt), and g', r', i' providing stars with V magnitude ranges from 7 to 17 mag (Henden & Munari 2014). Their latest catalog, DR9, covers almost 99% of the sky. For NGC 2345, we downloaded data from the APASS catalog.[9]

2.3. Comparison with Previous Photometry

The CCD $ubvy$ photometry down to $V \sim 18.0$ for the open cluster NGC 2345 has been discussed by Alonso-Santiago et al. (2019). We have performed a cross-identification of stars in the two catalogs, considering stars to be correctly matched when the positional difference is within one arcsecond. Based on these criteria, we have successfully identified 203 common stars. Figure 5 compares V magnitudes between the two catalogs. In the second column of Table 3, we list the difference between our V magnitude and that of Alonso-Santiago et al. (2019). This indicates that our V magnitude measurements agree with those provided in Alonso-Santiago et al. (2019).
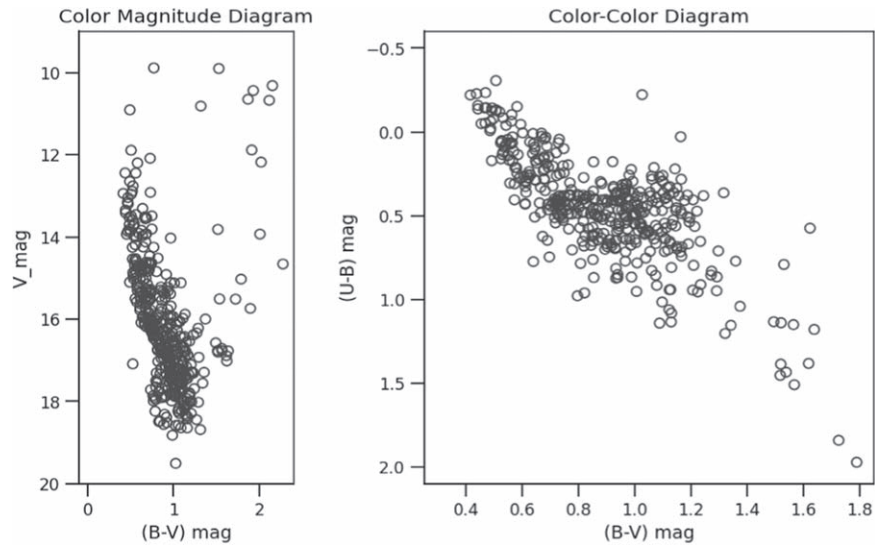

Figure 3. The $V/(B-V)$ color–magnitude and $(U-B)/(B-V)$ color–color diagrams of the cluster NGC 2345. A total of 426 stars observed in the present analysis are used for these diagrams.
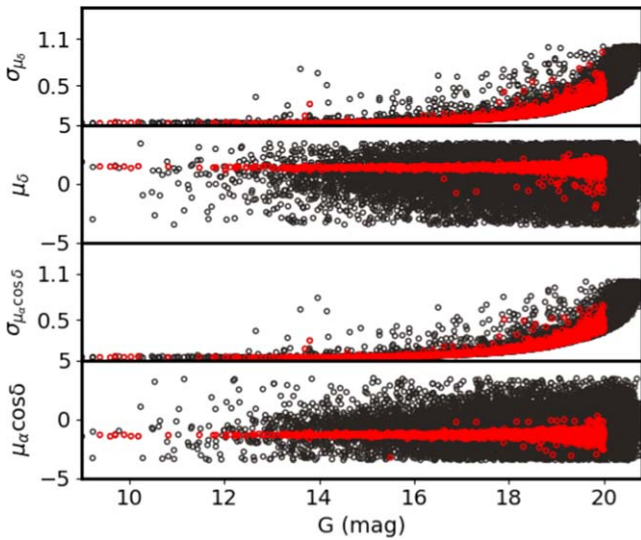

Figure 4. Plot of proper motions and their associated errors vs. G magnitude. The red empty circle symbols represents stars having membership probability $\geqslant 70\%$, and the black circle shows the field stars.
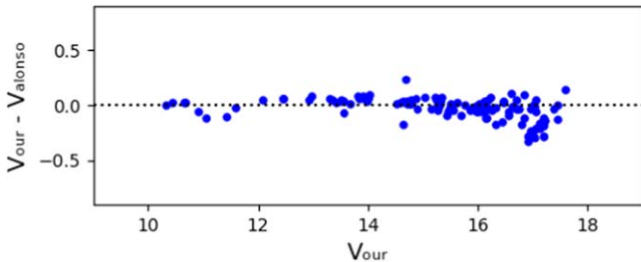

Figure 5. The blue dots on the graph represent the differences between our photometry and that of Alonso-Santiago et al. against V magnitude. The dotted line indicates zero difference.

Figure 6. Differences between measurements presented in the APASS catalog and this study for V magnitude and $(B-V)$ colors. The dotted line on the plot represents zero difference.

Table 3
Comparison of Our Photometry with Alonso-Santiago et al. (2019) and APASS Catalog

V	ΔV (Alonso)	ΔV (APASS)	$\Delta(B-V)$ (APASS)
10–11	0.00(0.03)	0.01(0.04)	0.15(0.14)
11–12	−0.08(0.04)	0.06(0.01)	0.02(0.01)
12–13	0.04(0.01)	0.01(0.01)	0.00(0.01)
13–14	−0.15(0.10)	0.05(0.10)	0.02(0.03)
14–15	0.02(0.16)	0.16(0.30)	0.04(0.04)
15–16	−0.07(0.28)	0.08(0.30)	0.01(0.13)
16–17	0.12(0.56)	⋯	⋯
17–18	0.20(0.96)	⋯	⋯

Note. The standard deviation in the difference for each magnitude bin is also given in parentheses.

2.4. Comparison with APASS Photometry

We conducted a cross-match between the current and APASS catalogs to compare photometry data. We considered a maximum positional difference of 1″.5 during the matching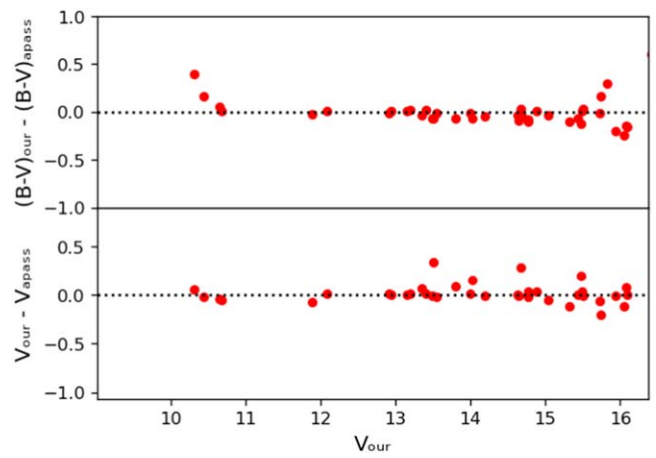 process. As a result, we identified 52 common stars in both catalogs. A comparison of V magnitudes and $(B-V)$ color between the two catalogs is plotted against V magnitude and shown in Figure 6. The results, including the mean differences and standard deviations in each magnitude bin, are listed in Table 3. The results of this comparison indicate a good
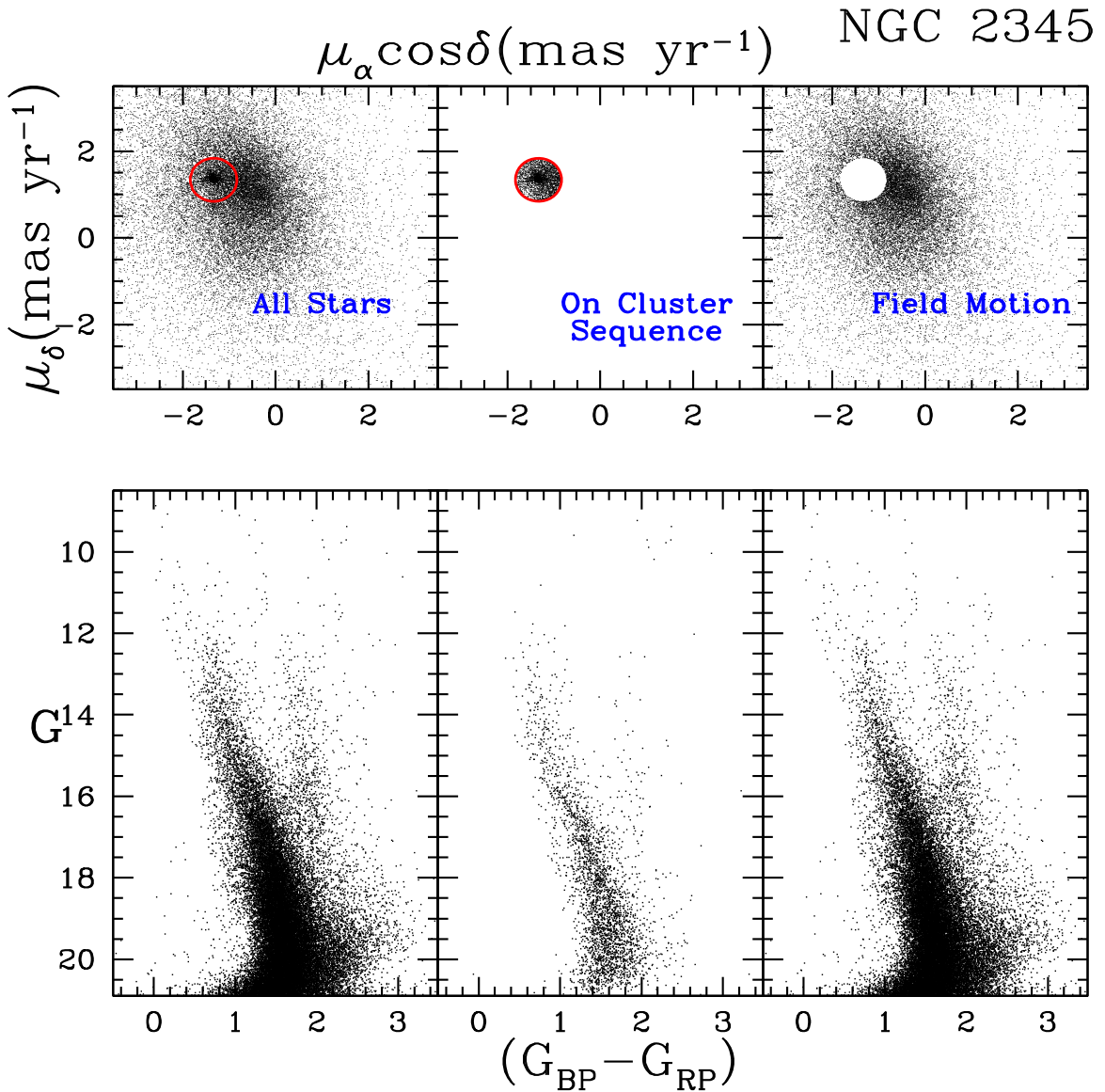
Figure 7. This figure shows the initial cluster member separation method using Gaia proper motions for the cluster. The top panel shows the vector point diagram and the bottom panels show the respective Gaia color–magnitude diagrams for the total stars, cluster members, and field stars. In the top panel, we have drawn a circle with a radius of $0.5 \, \mathrm{mas \, yr^{-1}}$ inside the cluster field, representing the member stars.

agreement between the V and $(B - V)$ measurements in our catalog and those provided in the APASS catalog.

3. Membership Probability

Most open clusters are found within the Galactic disk and are contaminated with numerous foreground and background stars. It is essential to distinguish between cluster members and nonmembers to obtain more accurate fundamental parameters for the cluster (Dias et al. 2018). We used the membership determination method described in Balaguer-Núnez et al. (1998) for the cluster NGC 2345. Many authors used this method in previous studies (Yadav et al. 2013; Sharma et al. 2020; Bisht et al. 2021a, 2021b, 2022a, 2022b). Proper-motion (PM) distribution is the unique identity of the stars or an excellent tool to separate the cluster members. In the PMs plane, cluster members are more concentrated than the field stars because member stars have similar properties. This method is purely based on the PM distribution of the

stars. The Gaia DR3 catalog offers unprecedented astrometric precision, enhancing reliability when determining cluster membership through kinematic data. As a result, we employed data from the Gaia DR3 archive for our kinematic analysis, membership determination, and distance calculations of the cluster. We considered probable cluster members selected from the vector point diagram (VPD) and color–magnitude diagram (CMD) to estimate the mean proper motion, as shown in Figure 7. A radius $0.5 \, \mathrm{mas \, yr^{-1}}$ circle around the center of the proper-motion distribution is drawn and assumed to contain cluster members. The remaining sources are considered field stars. We have displayed the CMD of the most probable members in the lower-middle panel, where the cluster's main sequence appears well defined for NGC 2345. The VPD based on the PMs in a zoomed-in view of the R.A. ($\mu_{\alpha*}$) and decl. (μ_δ) plane is shown in Figure 8, where $\mu_{\alpha*} = \mu_\alpha \cos(\delta)$.

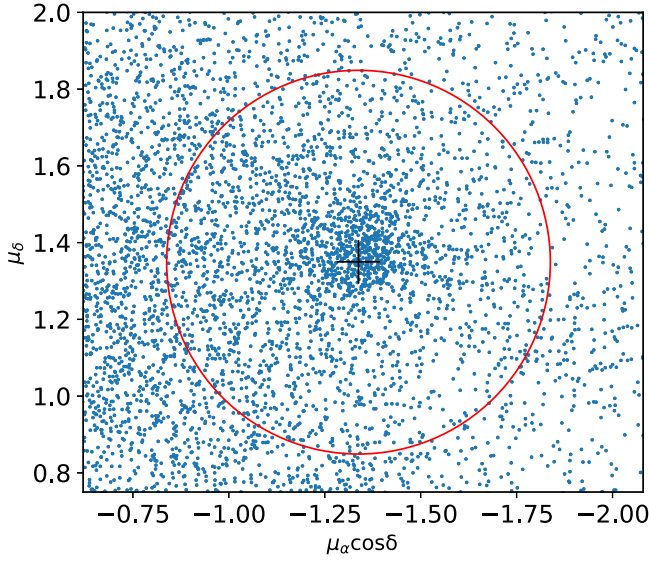In our selection method, we picked a star as the most probable member if it lies within the used radius in VPD,

Figure 8. A zoomed-in view of the proper-motion distribution of stars within a red circular area with a radius of 0.5 mas yr^{-1}. The plus sign denotes the proper-motion center.

having a PM error of $\leqslant 0.5$ mas yr^{-1} and a parallax within 3σ from the mean parallax of the cluster. The proper motions of the stars in the cluster region reach the maximum value at $(\mu_\alpha^*, \mu_\delta) = (-1.34, 1.35)$ mas yr^{-1}. We have used the approach discussed in Bisht et al. (2022a) to calculate the membership probability of the stars in the cluster region. We found the dispersion in PMs to be 0.08 mas yr^{-1} by using the cluster distance of 2.78 kpc and the radial-velocity dispersion of 1 km s^{-1} for open clusters (Girard et al. 1989). For field members, we have estimated $(\mu_{xf}, \mu_{yf}) = (1.3, -0.3)$ mas yr^{-1} and $(\sigma_{xf}, \sigma_{yf}) = (3.1, 2.9)$ mas yr^{-1}. These values are used to construct the frequency distributions of the cluster stars ($\phi_{\nu c}$) and field stars ($\phi_{\nu f}$) using the below equations described in Yadav et al. (2013) and Bisht et al. (2020):

$$\phi_c^\nu = \frac{1}{2\pi\sqrt{(\sigma_c^2 + \epsilon_{xi}^2)(\sigma_c^2 + \epsilon_{yi}^2)}}$$
$$\times \exp\left\{-\frac{1}{2}\left[\frac{(\mu_{xi} - \mu_{xc})^2}{\sigma_c^2 + \epsilon_{xi}^2} + \frac{(\mu_{yi} - \mu_{yc})^2}{\sigma_c^2 + \epsilon_{yi}^2}\right]\right\}$$

$$\phi_f^\nu = \frac{1}{2\pi\sqrt{(1-\gamma^2)}\sqrt{(\sigma_{xf}^2 + \epsilon_{xi}^2)(\sigma_{yf}^2 + \epsilon_{yi}^2)}}$$
$$\times \exp\left\{-\frac{1}{2(1-\gamma^2)}\left[\frac{(\mu_{xi} - \mu_{xf})^2}{\sigma_{xf}^2 + \epsilon_{xi}^2}\right.\right.$$
$$\left.\left. - \frac{2\gamma(\mu_{xi} - \mu_{xf})(\mu_{yi} - \mu_{yf})}{\sqrt{(\sigma_{xf}^2 + \epsilon_{xi}^2)(\sigma_{yf}^2 + \epsilon_{yi}^2)}} - \frac{(\mu_{yi} - \mu_{yf})^2}{\sigma_{yf}^2 + \epsilon_{yi}^2}\right]\right\}.$$

Here, (μ_{xi}, μ_{yi}) represents the PMs of the ith star, and $(\epsilon_{xi}, \epsilon_{yi})$ are the corresponding errors in the PMs. The coordinates (μ_{xc}, μ_{yc}) designate the PM center of the cluster, while (μ_{xf}, μ_{yf}) symbolize the PM center coordinates for field stars. The intrinsic proper-motion dispersion for cluster members is represented by σ_c, whereas σ_{xf} and σ_{yf} show the intrinsic proper-motion dispersions for field stars. The correlation

coefficient γ is calculated as:

$$\gamma = \frac{(\mu_{xi} - \mu_{xf})(\mu_{yi} - \mu_{yf})}{(\sigma_{xf}\sigma_{yf})}. \quad (4)$$

Finally, the membership probability for the ith star is eventually determined through the utilization of the following equation:

$$P_\mu(i) = \frac{n_c \times \phi_c^\nu(i)}{n_c \times \phi_c^\nu(i) + n_f \times \phi_f^\nu(i)} \quad (5)$$

where n_c and n_f are the normalized number of probable cluster members and field members, respectively. A plot of membership probability with G mag is shown in Figure 9. We have found 1732 stars with probability $\geqslant 70\%$, shown by red symbols in this figure. There is a clear separation between cluster stars and the field stars in the brighter end. At the fainter end ($G \sim 20$ mag), the separation between the stars gradually decreases. Most stars exhibiting high membership probability display a closely clustered distribution in the plot. We have used only those identified cluster members for further analysis in this paper.

4. Structural Parameters of the Cluster

Generally, open clusters consist of thinly dispersed and loosely bound stars, yet they exhibit the highest stellar density at their center. To estimate the center coordinate of the cluster NGC 2345, the Gaussian curve fitting provides the central coordinate as $\alpha = 107.08 \pm 0.07$ deg and $\delta = -13.20 \pm 0.08$ deg, which is shown in Figure 10. These values match the values given by Cantat-Gaudin et al. (2018).

The cluster radius (r_{cl}) is defined as the distance from the cluster center at which the average cluster contribution becomes negligible compared to the background stellar field. We utilize the stars' spatial surface density profile to estimate the cluster radius and assess the extent of field-star contamination. We achieve this by considering concentric circular regions around the estimated cluster center. Within each annular ring, typically with a width of approximately 70″, we count the stars and then divide this count by the respective areas of the annular rings to obtain the number density $\rho_i = N_i / A_i$, where N_i is the number of stars and A_i is the area of the ith zone. To derive the structural parameters, we fitted a surface density profile by King (1962) to the radial distribution of stars. This must be done using a nonlinear least-squares fitting, which uses the errors as weights.

Figure 11 displays the best-fit solution for the density distribution and its associated uncertainties. For the cluster, it decreases and flattens around $r_{cl} = 12′8 \pm 0′6$ and begins to merge with the field-star density. Therefore, we consider 12′8 as the cluster radius. A smooth dashed line represents a King (1962) profile:

$$f(r) = f_0 \left[\frac{1}{\sqrt{1 + (r/r_c)^2}} - \frac{1}{\sqrt{1 + (r_t/r_c)^2}}\right]^2 + f_b, \quad (6)$$

where f_b is the background density, f_0 is the central density, r_c is core radius, and r_t is the tidal radius. The core radius of a cluster can be defined as the distance from the cluster center at which the stellar density becomes half of the density at the cluster's center. The central density, background density, core radius, and tidal radius values are in Table 4.
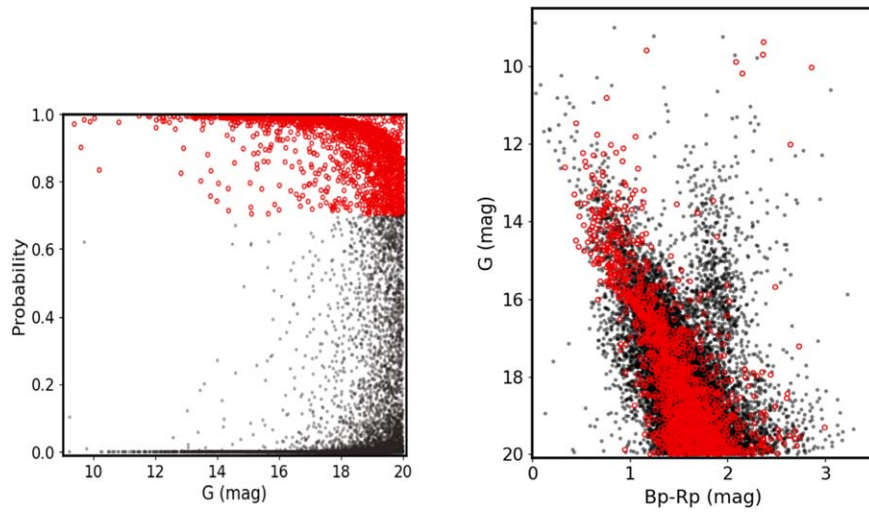
Figure 9. The Gaia membership probability is plotted as a function of *G* magnitude, with cluster members indicated by red empty circles with membership probability higher than 70%. The distribution of stars in the CMD is shown in the right panel.
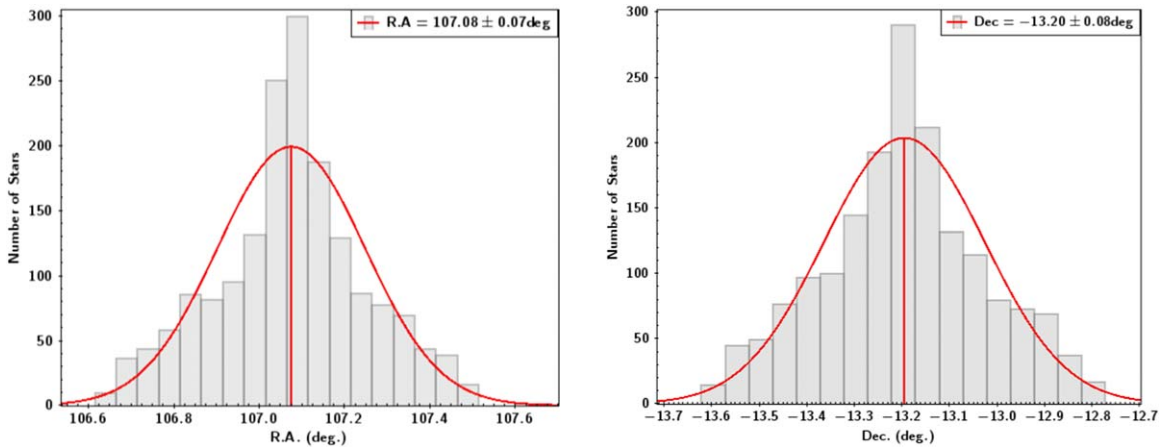

Figure 10. Stellar count profiles across the cluster region have been analyzed using Gaussian fits. The center of symmetry about the peaks of R.A. and decl. is the position of the cluster's center.
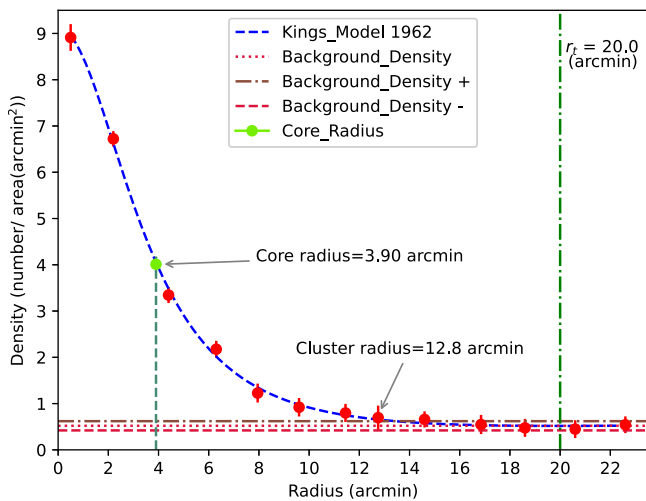

Figure 11. The radial density profile for the cluster. The best-fit blue curve represents the King (1962) profile, from which we obtained both the core (r_c) and the tidal (r_t) radius. Their positions are indicated with vertical dashed lines. The horizontal lines represent the stars' background density and the corresponding errors.

Table 4
Structural Parameters of the Cluster under Study

Central Density (f_0)	10.12 ± 0.98 number arcmin^{-2}
Background Density (f_b)	0.51 ± 0.04 number arcmin^{-2}
Core Radius (r_c)	$3'.9 \pm 0'.2$
Tidal Radius (r_t)	$20'.0 \pm 2'.1$
Cluster Radius (r_{cl})	$12'.8 \pm 0'.6$

5. Reddening of NGC 2345

The plots of two-color diagrams (TCDs) for various pairs of colors serve as valuable tools for estimating interstellar reddening and gaining insights into the properties of the extinction law in the direction of the clusters.

5.1. (U − B)/(B − V) Color–Color Diagram

Knowledge of reddening is crucial for determining the intrinsic properties of cluster stars. In cases where spectroscopic observations are unavailable, we can rely on color–color diagrams such as $(B - V)$ and $(U - B)$ to estimate the reddening of clusters, as demonstrated by Becker & Stock (1954). To estimate the
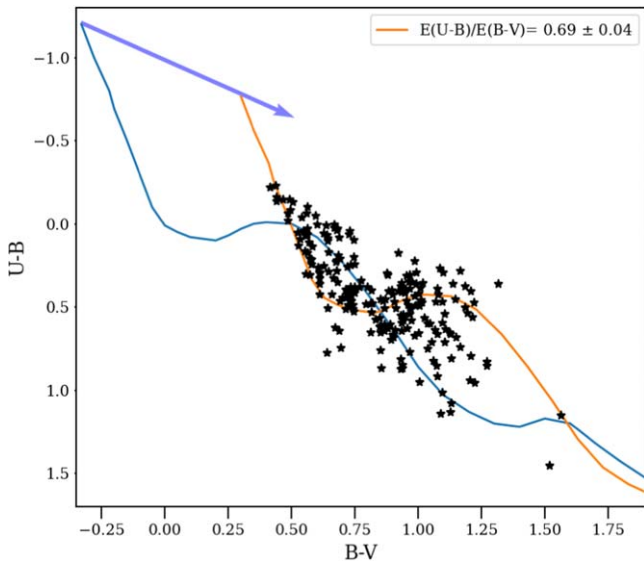
Figure 12. The $(U - B)$ vs. $(B - V)$ color–color diagram for NGC 2345. We have used only cluster members with membership probability higher than 70%. The arrow indicates the reddening vector.
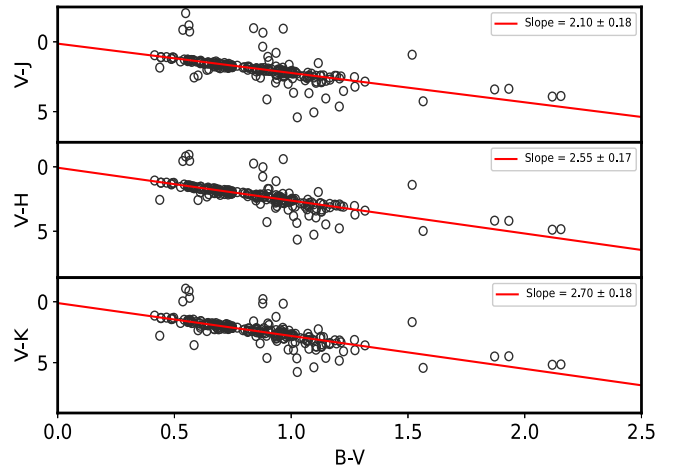

Figure 13. The $(V - \lambda)/(B - V)$ diagrams for member stars in the cluster NGC 2345. The continuous lines represent the slope determined through the least-squares linear fit and are mentioned in each panel.

Table 5
The Color-excess Ratios Observed toward NGC 2345 and the Standard Values from Cardelli et al. (1989)

NGC 2345	$(V - J)/(B - V)$	$(V - H)/(B - V)$	$(V - K)/(B - V)$
Observed ratio	2.10 ± 0.18	2.55 ± 0.17	2.70 ± 0.18
Normal ratio	2.30	2.58	2.78

interstellar extinction toward the clusters, we created a $(U - B)$ versus $(B - V)$ diagram utilizing 233 identified cluster members, cross-referenced with Gaia data as illustrated in Figure 12.

We acquired a reddening vector slope of $\frac{E(U - B)}{E(B - V)}$ and aligned it with the intrinsic zero-age main sequence (ZAMS) of 0.01 metallicity based on Schmid-Kaler (1982) for main-sequence stars. We adjusted the ZAMS to the brighter stars to account for varying color excesses. The optimal fit, associated with $E(B - V) = 0.63 \pm 0.04$ mag, is illustrated with the orange curve. The estimated $E(B - V)$ value shows good agreement with $\sim 0.66 \pm 0.13$ obtained by Alonso-Santiago et al. (2019).

5.2. Total-to-selective Extinction Value

Reddening is crucial for determining the fundamental parameters of clusters, such as age and distance. To ascertain the characteristics of the extinction law, it is essential to examine the TCD. Photons emitted by the cluster stars that pass through the interstellar medium are absorbed and scattered by the medium's dust, gas, and molecular clouds. The normal Galactic reddening law frequently does not apply along the line of sight to clusters (Sneden et al. 1978).

Chini et al. (1990) suggested $(V - \lambda)$ versus $(B - V)$ TCDs to examine the nature of the reddening law, where λ denotes the filter other than V mag reddening law. Here, λ denotes the magnitude with the filter at that wavelength. We have studied the reddening law for the cluster by creating TCDs in the three 2MASS filters, as shown in Figure 13. A linear dependence is observed among the stellar color values. The slope ($m_{cluster}$) for each TCD is calculated by least-squares fitting as shown by the solid lines in Figure 13 and tabulated in Table 5 with corresponding normal values. This table shows that the estimated color-excess values align well with the expected normal values.

The extinction ($R_{cluster}$) toward the cluster is calculated by the following equation:

$$R_{cluster} = \frac{m_{cluster}}{m_{normal}} \times R_{normal}, \qquad (7)$$

where R_{normal} is the normal value of the total to selective extinction ratio, and $m_{cluster}$ and m_{normal} are the estimated and normal slopes in the TCD, respectively. By assuming the value of R_{normal} as 3.1, we calculated $R_{cluster}$ in the different passbands to be $3.1 \leqslant R \leqslant 3.4$, which is close to the normal value. Hence, the reddening law is similar to that of the general interstellar medium within the cluster region.

5.3. Interstellar Reddening from JHK Colors

The near-IR photometry is important to understand the nature of interstellar extinction (Tapia et al. 1988). The wavelengths in the near-IR region are longer than in the visible spectrum. Therefore, the near-IR provides information about types of dust that have larger particle sizes compared to visible-wavelength dust. As in the previous section, we have utilized 2MASS data in the JHK photometry bands to investigate the interstellar extinction law. The $(J - K)$ versus $(J - H)$ diagram is presented in Figure 14.

The ZAMS of 0.01 metallicity, depicted as the solid line, is adopted from Caldwell et al. (1993). The visual fitting of the ZAMS yields $E(J - H) = 0.20 \pm 0.04$ mag and $E(J - K) = 0.34 \pm 0.03$ mag. The ratio $\frac{E(J - H)}{E(J - K)}$ is found to be 0.59 ± 0.04, which shows a good agreement with the normal interstellar extinction value of 0.55 suggested by Cardelli et al. (1989). The reddening is calculated using the following equations (Fiorucci & Munari 2003):

$$E(J - H) = 0.309 \times E(B - V)$$
$$E(J - K) = 0.480 \times E(B - V). \qquad (8)$$

We found the interstellar reddening of the cluster to be 0.68 ± 0.10, calculated by averaging the results from both equations, yielding individual values of 0.65 ± 0.13 and
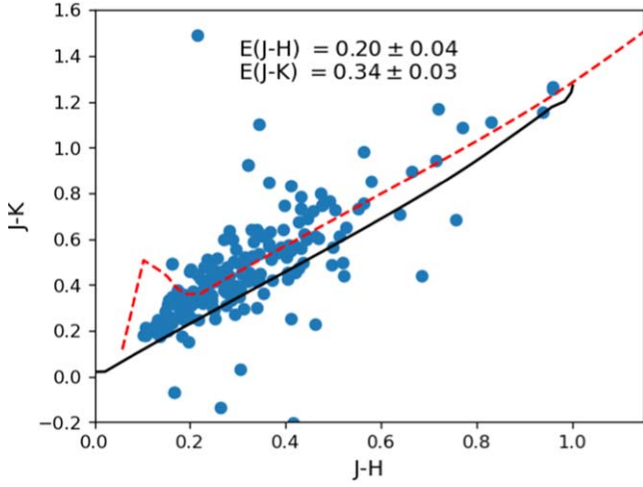
Figure 14. The plot of $(J - K)$ vs. $(J - H)$ color–color diagram. Solid and dotted lines are the ZAMS taken from Caldwell et al. (1993).
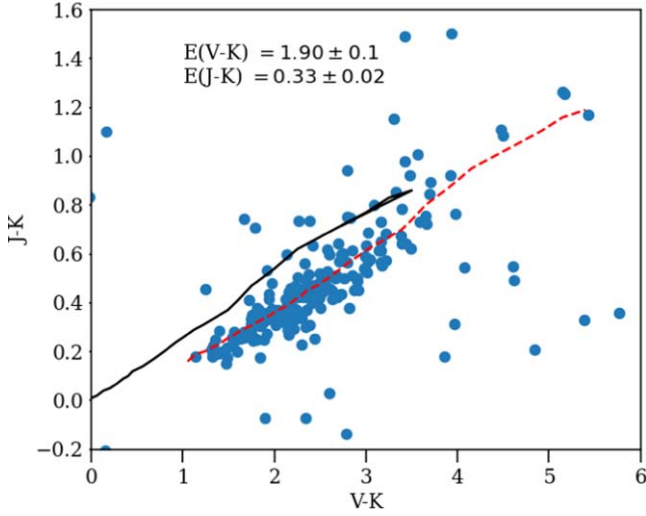

Figure 15. The plot of $(V - K)$ vs. $(J - K)$ color–color diagram. Solid and dashed lines are the ZAMS taken from Caldwell et al. (1993).

0.71 ± 0.06. The $E(B - V)$ values derived from the near-IR TCDs reconfirm our finding of the $E(B - V)$ value estimated from the optical $E(U - B)/E(B - V)$ TCDs. We have also calculated the value of $\frac{E(J - K)}{E(V - K)} = 0.17 \pm 0.06$, which is in good agreement with the normal interstellar extinction value of 0.19 given by Cardelli et al. (1989), as shown in Figure 15.

6. Distance and Age of the Cluster

6.1. Distance Estimation Using Parallax

We employed the method proposed by Luri et al. (2018), which involves estimating the distance of a cluster using its average parallax value. Because of the inherent errors in the parallax data from Gaia DR3, we computed their weighted mean by considering the probable cluster member stars. The parallax values from Gaia have negative values due to minimal angles, hence they are indicators of large distances (Astraatmadja & Bailer-Jones 2016). Since the open clusters of the Galaxy are not that distant, we generated a histogram of the parallax values of cluster members, excluding stars with negative parallax values. We determined the mean parallax
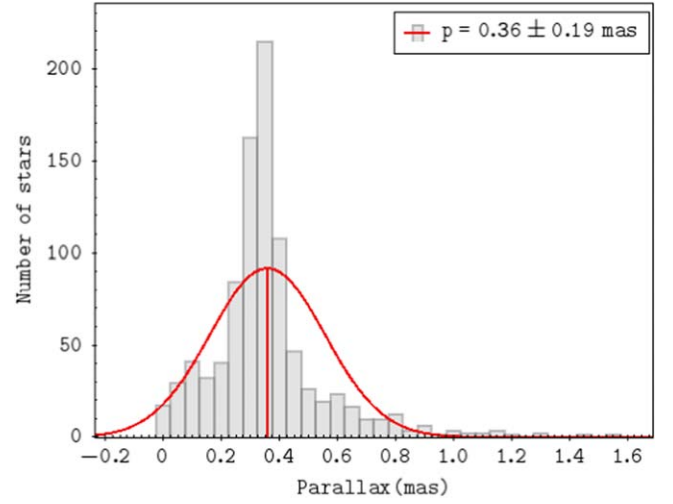

Figure 16. Plot of the histogram of parallax. The Gaussian function is fitted to the central bins and provides the mean value of parallax.

angle for the cluster by fitting Gaussian curves to the histograms. The plot for the histogram with a Gaussian fit is presented in Figure 16.

We estimated the mean parallax as 0.36 ± 0.19 mas and then computed the cluster distance by taking the reciprocal of the mean parallax after applying a zero-point offset of -0.021 mas to the mean parallax as suggested by Groenewegen (2021). We obtained a distance of 2.77 ± 0.11 kpc. The parallax estimation by Gaia is associated with the corresponding errors; hence, the distance calculated by inverting the parallax can give the wrong estimation. Bailer-Jones (2015) proposed a probabilistic analysis–based method for determining distances, which offers a more precise estimate than the distance obtained through parallax inversion. They used the Bayesian approach to calculate the distance of a star having a parallax and associated error measurements. For this, they tested different priors and concluded that an exponentially decreasing space density prior and Milky Way priors are best among all. We have computed distances using the approach outlined in Bailer-Jones et al. (2018). The calculated distance is 2.78 ± 0.78 kpc, slightly higher than $\sim$2.652 kpc obtained by Cantat-Gaudin et al. (2020).

6.2. Age and Distance from Isochrone Fitting

CMDs illustrate the correlation between the absolute magnitudes of stars and their surface temperatures, typically identified by their colors. CMDs are widely employed for studying star clusters and prove valuable for estimating their properties (Kalirai & Tosi 2004; Sariya et al. 2021). We used the most probable member stars of NGC 2345 to generate the CMDs. Analyzing the morphology of CMDs helps identify the key features such as the main sequence, turnoff point, and giant members, ultimately leading to model-based mass, age, and distance estimations for each star (Bisht et al. 2019). In this study, we simultaneously estimated the distance modulus and age by fitting the theoretical isochrones given by Marigo et al. (2017) to the UBV, Gaia, and 2MASS-based CMDs of the cluster. To determine the distance modulus and age, as well as the distance of the cluster, we constructed $V \times (B - V)$, $V \times (U - B)$, $V \times (V - K)$, $V \times (J - K)$, $J \times (J - H)$, and $G \times (G_{BP} - G_{RP})$ diagrams and visually fitted the isochrones (Marigo et al. 2017) by only considering the probable members
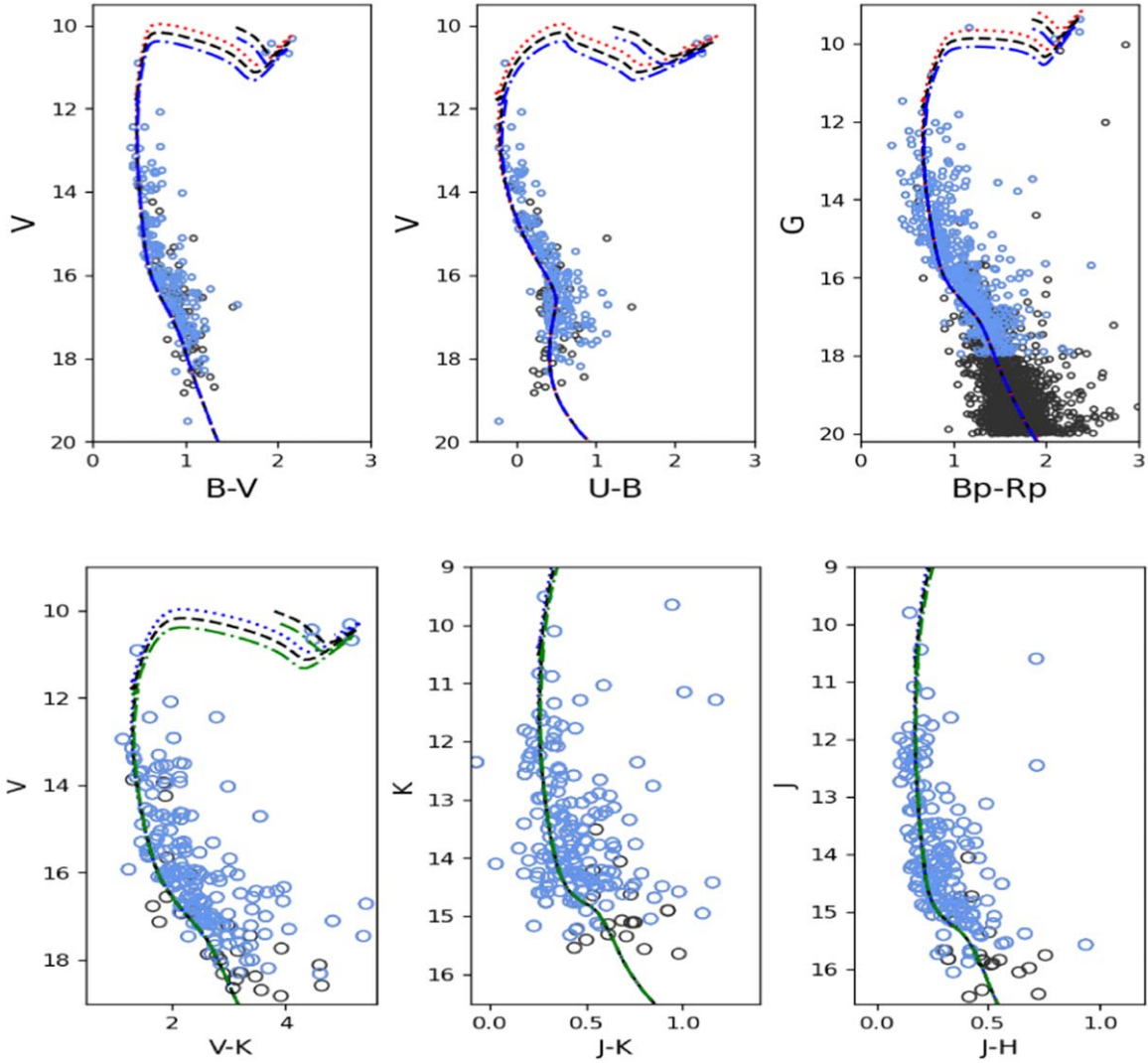
Figure 17. The optical and near-IR color–magnitude diagram of the cluster under study. The curves are the isochrones of log(age) = 7.75, 7.8, and 7.85. These isochrones are taken from Marigo et al. (2017). Black circles are the probable cluster members identified in the present study, while the light-blue circles represent the matched stars with the Cantat-Gaudin et al. (2020) catalog.

($P \geqslant 0.7$). We attempted to fit numerous isochrones with varying metallicity and ages and determined the best fit at $Z = 0.01$. We employed the magnitudes of stars in different filters to ensure a reliable determination of cluster properties via isochrone fitting. The $E(B - V)$ value is taken from Section 5 for the isochrone-fitting procedure in *UBV* filters. For Gaia DR3 filters, we used the relation $E(G_{BP} - G_{RP}) = 1.41 \times E(B - V)$ given by Sun et al. (2021) to convert $E(B - V)$ into $E(G_{BP} - G_{RP})$. The calculated color-excess value, $E(G_{BP} - G_{RP})$ for the cluster is 0.89 mag. Uncertainties in age were determined by utilizing both low- and high-age isochrones, which were selected to best fit the observed scatter around the main sequence (MS) shown in Figure 17.

We superimposed theoretical isochrones of different ages (log (age) = 7.75, 7.8, and 7.85 with z = 0.01) on the different CMDs to obtain the distance modulus and age. There are a few giants present in this cluster. The fitted isochrones also pass through the giant stars, clearly illustrating the cluster's evolutionary path. In this way, we estimated the cluster's age to be 63 ± 8 Myr with a true distance modulus $(m - M)_0 = 12.0 \pm 0.2$ mag. The corresponding heliocentric distance, calculated through the distance

modulus, is 2.51 ± 0.12 kpc. The distance calculated using distance modulus is compatible with Gaia DR3 parallax distance measurement of the present study as well as the values reported by Cantat-Gaudin et al. (2018) and Alonso-Santiago et al. (2019) within a margin of errors. The A_V value for cluster members was computed using the weighted mean method based on the CCD *UBV* data. Adopting $R_V = 3.1$, the value A_V for this cluster is 1.95 ± 0.12, which is consistent with the value of 1.91 reported by Tsantaki et al. (2023). A comparative analysis of the fundamental properties of cluster members, as determined in this study, is presented alongside values found in the existing literature in Table 6. We have determined the Galactocentric coordinates of the cluster to be $X_{GAL} = -1.887$ kpc, $Y_{GAL} = -1.994$ kpc, and $Z_{GAL} = -0.111$ kpc. The estimated Galactocentric distance is $R_{GC} = 10.4$ kpc. The above parameters are in fair agreement with the values obtained by Cantat-Gaudin et al. (2020). Such information is essential for studying the cluster's environment, its motion within the Galaxy, and its interaction with other Galactic components. Additionally, Galactocentric coordinates provide a foundation for broader astrophysical investigations, aiding in the contextual understanding of the cluster's role in the dynamic structure of the Milky Way.

Parameters	Numerical Values	Reference
R.A., decl. (deg)	$(107.08 \pm 0.07, -13.20 \pm 0.08)$	Present work
	$(107.075, -13.199)$	Cantat-Gaudin et al. (2020)
	$(107.085 \pm 0.007, -13.197 \pm 0.008)$	Alonso-Santiago et al. (2019)
	$(107.075, -13.197)$	Carraro et al. (2015)
$\mu_\alpha \cos\delta, \mu_\delta$ (mas yr^{-1})	$(-1.34 \pm 0.20, 1.35 \pm 0.21)$	Present Work
	$(-1.33 \pm 0.10, 1.34 \pm 0.11)$	Carrera et al. (2022)
	$(-1.332, 1.340)$	Cantat-Gaudin et al. (2020)
	$(-1.36 \pm 0.10, 1.33 \pm 0.09)$	Alonso-Santiago et al. (2019)
Cluster Radius (arcmin)	12.8	Present Work
	3.75	Carraro et al. (2015)
	7.2	Kharchenko et al. (2005)
	5.25	Moffat (1974)
Age (Myr)	63 ± 8	Present Work
	56 ± 13	Alonso-Santiago et al. (2019)
	79.4	Holanda et al. (2019)
	63-70	Carraro et al. (2015)
	77.4	Kharchenko et al. (2005)
	78.5	Dias et al. (2002)
	60	Moffat (1974)
Mean Parallax (mas)	0.36 ± 0.19	Present Work
	0.35 ± 0.05	Carrera et al. (2022)
	0.348	Cantat-Gaudin et al. (2020)
	0.35 ± 0.03	Alonso-Santiago et al. (2019)
Distance (kpc)	2.78 ± 0.78	Present Work
	2.662	Carrera et al. (2022)
	2.652	Cantat-Gaudin et al. (2020)
	2.5 ± 0.2	Alonso-Santiago et al. (2019)
	2.251	Kharchenko et al. (2005)
	1.750	Moffat (1974)

7. Dynamical Study

7.1. Luminosity and Mass Function

The luminosity function (LF) characterizes the distribution of stars within a cluster according to their luminosities. The LF for main-sequence stars within the cluster is derived from the calculated properties of the probable cluster stars. To construct the LF, we only considered the stars having membership probability $\geqslant 70\%$. The apparent G magnitudes of these stars are converted to their absolute magnitudes using the distance modulus and A_G ($=1.66$ mag). The magnitude bin interval of 1.0 mag was chosen to get a sufficient number of stars per magnitude bin for good statistics. Then, we constructed the histogram of LFs for the cluster, as shown in Figure 18. We found an increasing LF for this cluster.

The mass function (MF) describes the distribution of masses among members of a cluster within a unit volume, and a mass–luminosity relationship can convert the LFs into the MF. Converting a cluster's LFs into the mass function involves utilizing best-fit theoretical evolutionary tracks, as shown in Figure 19.

We have utilized the theoretical models provided by Marigo et al. (2017) for this conversion. Through a least-squares-fitting approach, we determined the slope of the distribution by fitting the following equation:

$$\log \frac{dN}{dM} = -(1 + x) \times \log(M) + \text{constant}. \qquad (9)$$

In the above relation, dN is the number of stars in a particular mass bin dM, and x is the slope of a mass function. The mass

function slope was calculated for the cluster in three regions, i.e., the core, halo, and entire cluster region. The parameters of the cluster are taken from the Section 4. The slope values of the mass function are listed in Table 7.

The mass function slope is steeper for the core region, while for the entire cluster region, the slope is slightly lower than the Salpeter value of $x = 1.354$ (Salpeter 1955). By contrast, the halo region exhibits good agreement with the Salpeter value. Furthermore, it is observed that the mass function slopes tend to increase as one moves toward the outer regions of the cluster compared to the core region. It may be because massive stars tend toward the cluster core while faint stars move toward the halo and outer region, and a possible hint of mass segregation is described in the next section.

7.2. Mass Segregation

Open clusters are known to have mass segregation (Dib et al. 2018; Dib & Henning 2019). Mass segregation is the concentration of bright and massive stars toward the cluster's central region rather than of the faint and low-mass stars. It is still a topic of debate whether mass segregation is primarily a result of the dynamical evolution of the cluster, the star formation process itself, or a combination of both (Dib et al. 2018; Plunkett et al. 2018). During the dynamical evolution of clusters, massive stars undergo kinetic energy transfer to low-mass stars through the process of equipartition of energy, leading to an accumulation of massive stars in the central region of the cluster, while low-mass stars gradually migrate toward the outer region (Allison et al. 2009). This process occurs because of the star formation process, which results in
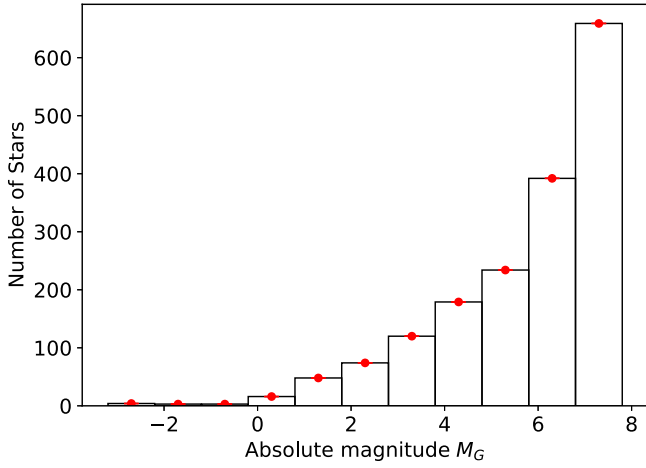
Figure 18. Histogram representing the distribution of main-sequence stars within each specified magnitude bin, with M_G denoting the absolute magnitude and red dots representing the associated errors.
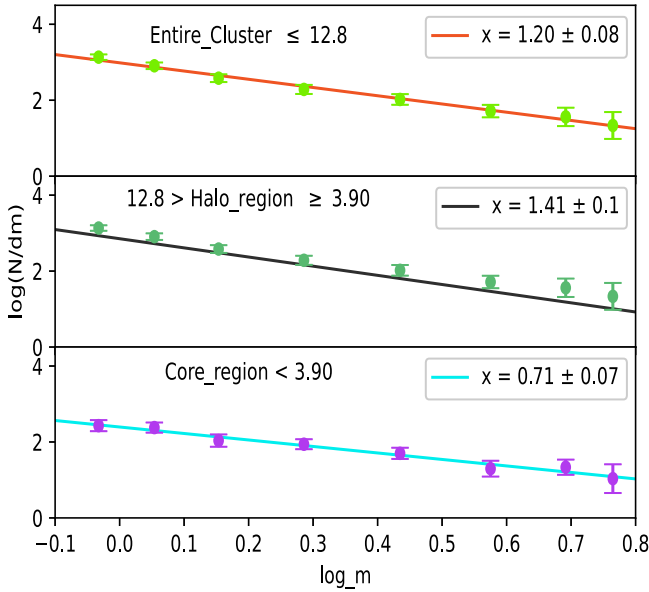

Figure 19. The mass function slope for NGC 2345 in three regions: core, halo, and cluster region. The slope of the mass function is calculated by least-squares fitting, as shown by solid lines in each panel.

Table 7
The Mass Function Slope Values for Different Cluster Regions

Cluster	NGC 2345
Mass Range ($M_\odot$)	$0.84 - 6.2$
Mass Function Slope (x)	...
Core	0.70 ± 0.07
Halo	1.41 ± 0.10
Entire Region	1.20 ± 0.08

the preferential formation of massive stars in the central region of the cluster (Dib et al. 2007, 2010). Studying young open clusters is important for investigating the mass segregation process during dynamical evolution and its association with star formation (Pavlík et al. 2019). We create a cumulative distribution of stars based on their radial distance to study mass segregation within the cluster. We derived the cumulative radial stellar distribution of member stars for different
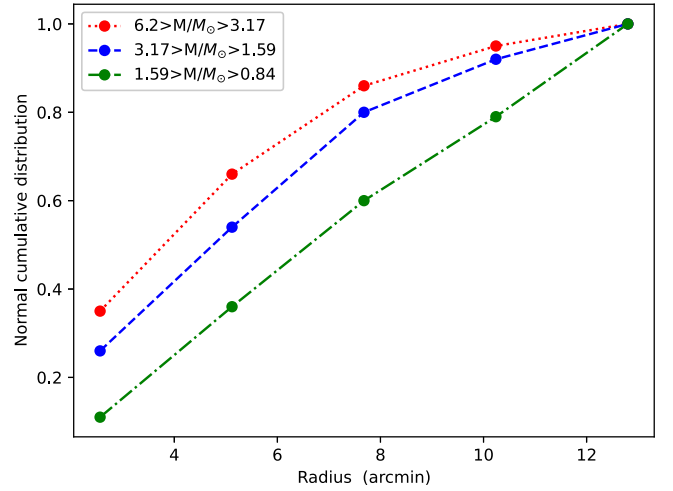

Figure 20. The cumulative radial distribution of stars in different mass ranges. The orange dotted line, blue dashed line, and green dashed dot line correspond to the high-, intermediate-, and low-mass ranges, respectively. The mass ranges are mentioned in the upper left of the graph.

mass ranges, as shown in Figure 20. We considered high-, intermediate-, and low-mass ranges, as indicated in Figure 20. We also conducted the Kolmogorov–Smirnov test on these mass ranges to determine whether they represent statistically different samples. We conclude with a confidence level of 80% that the mass segregation effect is present in the cluster NGC 2345.

7.3. The Dynamical Relaxation Time

The relaxation time provides a meaningful measure of the timescale over which a cluster will lose any remnants of its initial conditions. The relaxation timescale is characterized when a cluster reaches equipartition energy. The relaxation time given by Spitzer & Hart (1971) is described by the following equation:

$$T_E = \frac{8.9 \times 10^5 N^{1/2} R_h^{3/2}}{\langle M \rangle^{1/2} \log(0.4N)}. \tag{10}$$

Here, N is the number of member stars, R_h is the half-mass radius (in pc) of the cluster, and $\langle M \rangle$ is the mean mass of the member stars in units of solar mass. The relaxation time in years, denoted as T_E, is determined based on the calculation of R_h, derived by considering the cumulative mass of stars as radial distance increases outward from the cluster center. R_h represents the radial distance where half of the total cluster mass is contained. We have calculated the value of R_h based on the transformation equation as given in Larsen (2006),

$$R_h = 0.547 \times R_c \times \left(\frac{R_t}{R_c} \right)^{0.486}$$

where R_c is the core radius and R_t is tidal radius, and we have used those values from our estimation presented in this paper. We found the R_h value to be $8.'65 \pm 0.'20$ (6.97 ± 0.16 pc) and the corresponding T_E value to be 177.6 Myr for the cluster. The cluster exhibits a relaxation time (T_E) that exceeds its current age; therefore, mass segregation in NGC 2345 prompts speculation regarding its potential association with the star formation process. Indeed, the early occurrence of mass

Table 8
The Calculated Dynamical Parameters for NGC 2345

Cluster Parameter	NGC 2345
Member stars	1732
Mean stellar mass ($M_\odot$)	1.826
Total mass ($M_\odot$)	3163
Cluster half radius (R_h pc^{-1})	6.97 ± 0.17
Relaxation time (T_E Myr^{-1})	177.6

segregation in clusters can be attributed to the rapid dynamical evolution that takes place, even within very young clusters, as suggested by certain previous studies (McMillan et al. 2007; Allison et al. 2009). The cluster parameters found from the dynamical study of the open cluster NGC 2345 are listed in Table 8.

7.4. Apex of the Cluster

The apex position shows the movement of star clusters across the celestial sphere. An OC is a gravitationally bound system of stars where the cluster members move with a shared velocity vector. Determining the apex position in OCs is paramount as it unveils crucial insights into the collective motion and dynamics of the cluster members across the celestial sphere. The methods described are based on the assumption that a cluster is a nonrotating body without any expansion or contraction (Maurya et al. 2021). The apex, obtained through the AD diagram method utilizing radial-velocity and parallax measurements, is a critical parameter for understanding these clusters' kinematics, Galactic dynamics, and formation history. It not only aids in deciphering the common origin of cluster members from a molecular cloud but also contributes to broader studies of the Milky Way's structure and the dynamics of stellar systems within it. We have used the AD diagram method to obtain the apex of the cluster. This method uses radial-velocity measurements and parallaxes of the stars. The AD diagram is discussed in detail by Chupina et al. (2001, 2006), Vereshchagin et al. (2014), Elsanhoury et al. (2018), and Postnikova et al. (2020). The (A, D) values of individual member stars indicate the positions of these stars through space velocity vectors. In this method, the intersection point $(A_\emptyset, D_\emptyset)$, also referred to as the apex in equatorial coordinates, can be expressed as follows.

$$A_\emptyset = \tan^{-1}\left[\frac{\bar{V_y}}{\bar{V_x}}\right], \qquad D_\emptyset = \tan^{-1}\left[\frac{\bar{V_z}}{\sqrt{\bar{V_x^2} + \bar{V_y^2}}}\right]. \quad (11)$$

Here, V_x, V_y, and V_z represent the spatial velocities of stars on the celestial sphere. We have utilized the equation provided in Chupina et al. (2001) to calculate the velocity components. We determined the coordinates of the apex $(A_\emptyset, D_\emptyset)$ using the AD diagram method, which were calculated as $(-40°.89 \pm 0.12, -44°.99 \pm 0.15)$. Our estimated kinematical parameters are crucial for understanding the complete picture of a star's space motion within the cluster. This method uses the radial velocities and parallaxes of the Gaia 1732 stars with membership probability higher than 70% (Figure 21).
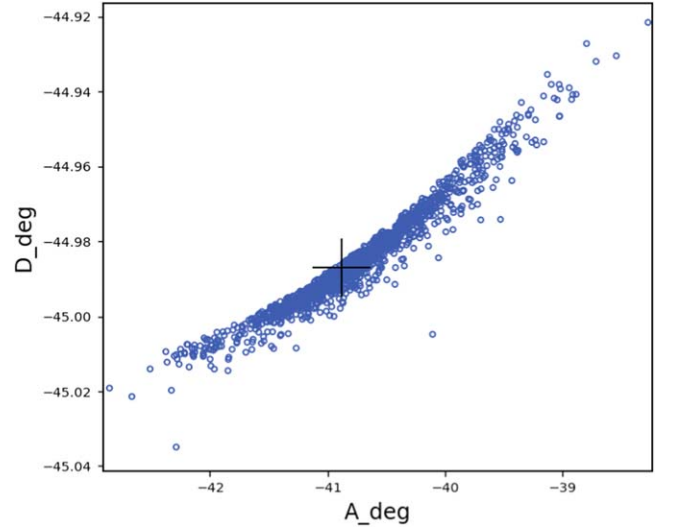

Figure 21. AD diagram for cluster NGC 2345. All stars (1732) are probable members with a membership probability higher than 70%. A plus sign indicates the mean value of apex coordinates, described in the text.

7.5. Motion of the Cluster in the Galaxy

To study the influence of the Galactic dynamics on the evolution of the cluster NGC 2345, we back-traced its motion in the Galaxy. Since the actual mass distribution of the Galaxy is unknown, we used the available mass models of the Galaxy. For this analysis, we used the most reliable Galactic potential model given by Allen & Santillan (1991). This model assumes that the total mass of the Galaxy is divided into three components: a central bulge, disk, and halo. The potential for the bulge and disk are taken from Miyamoto & Nagai (1975), and for the halo region the potential from Wilkinson & Evans (1999) is used. For this analysis, we used the updated parameters calculated by Bobylev et al. (2017) using data from different sources up to a Galactocentric distance of 200 kpc. This model is widely used and discussed in many studies such as Bisht et al. (2019) and Rangwal et al. (2019). To perform the back integration of the orbital path of the cluster in the Galaxy, we transformed the position and velocity components given in Table 6 into Galactocentric coordinates. This analysis takes the cluster's radial velocity from Alonso-Santiago et al. (2019) as 58.41 ± 0.15 km s^{-1}. We used the transformation matrices given by Johnson & Soderblom (1987), and the coordinates of the Galactic North Pole and Galactic Center from Reid & Brunthaler (2004). The results of this transformation, the Galactocentric position and velocity of the cluster, are listed in Table 9. The radial components are taken positively toward the Galactic Center, the tangential component is positive toward the Galactic rotation, and the vertical component is positive toward the Galactic North Pole.

We back-integrated the orbits for a time equal to the cluster's age, as shown by the red curve in Figure 22. Due to a very young age, the cluster has not completed one revolution around the Galactic Center; hence, we integrated the orbit for 300 Myr to determine the orbital properties of the cluster. The first panel from the left shows a plot between radial distance from the Galactic Center and scale height from the Galactic disk. This plot shows that the cluster is orbiting outside the solar circle with a maximum scale height of 0.1 kpc, which makes it an object of the thin Galactic disk. The green triangles in these plots represent the birth position, and the red circle is the
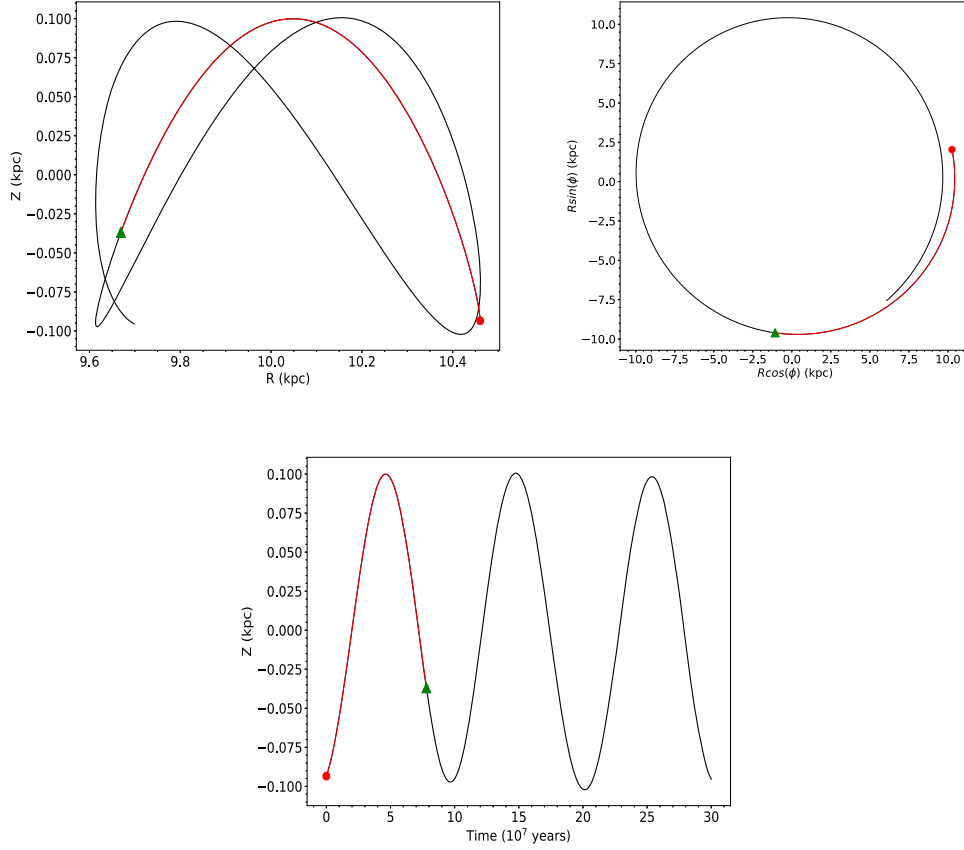
Figure 22. Galactic orbit of the NGC 2345 estimated with the Galactic potential model described in the text in the time interval of the cluster's age. The top-left panel shows a side view and the right panel shows a top view of the cluster's orbit. The bottom panel shows the motion of NGC 2345 in the Galactic disk with time. The filled triangle and filled circle denote the birth and present-day position of the cluster in the Galaxy.

Table 9
Spatial and Velocity Coordinates of NGC 2345 in the Galactocentric Coordinates, with Orbital Parameters

Parameter	NGC 2345
(R, Z); (kpc)	$(10.46 \pm 0.79, -0.09 \pm 0.04)$
U (km s^{-1})	-0.53 ± 7.22
V (km s^{-1})	-235.16 ± 7.15
W (km s^{-1})	2.41 ± 7.14
eccentricity	0.001
(R_A, R_P); (kpc)	$(10.44, 10.42)$
Z_{max} (kpc)	0.10
Energy (100 km s^{-1})^2	-09.85
L_Z (100 kpc km s^{-1})	-24.60
Time period (Myr)	278

Note. R is the radial distance from the Galactic Center, Z is the vertical distance of the cluster from the Galactic disk, and U, V, and W are the velocities of the clusters in radial, tangential, and vertical directions, respectively. Z_{max} is the maximum distance the cluster travels from the Galactic disk. R_A and R_P are apogalactic and perigalactic radii of the orbit, respectively. L_Z is the third component of the angular momentum.

present-day position of the cluster. It is visible that the cluster was born very close to the Galactic disk; hence, it is highly affected by the Galactic tidal forces, which is indicate by the close proximity of the cluster orbit to the Galactic disk. This close proximity will affect the evolution and survival of the cluster stars in the Galaxy. The increasing signature of the luminosity function shown in Figure 18 depicts that most of the cluster's low-mass stars are bound to the cluster, which is due to its early age, but with time we can predict that the stars will merge into the field distribution with a faster rate. The top-right panel of Figure 22 shows the plot between the components of the radial distance of the cluster. This plot shows that the cluster follows a circular path in the Galaxy while moving around the Galactic Center. The bottom panel of this figure shows a plot between the time of motion and the perpendicular distance, which shows that the cluster is moving up to the same vertical height as the disk. This signifies that the cluster faces the same force across its path from the disk.

8. Summary and Conclusions

We thoroughly analyze the young open cluster NGC 2345 through photometric and kinematic studies. Our investigation is based on *UBV* data from the 2.0 m Himalayan Chandra telescope, complemented by valuable insights from Gaia DR3, 2MASS, and APASS data. The findings of our study are summarized as follows.

1. We have estimated the cluster center with high precision using the cluster members and found the following coordinates: $\alpha = 107°.08 \pm 0°.07$ (07^{h}08^{m}8^s.3) and $\delta = -13°.20 \pm 0°.08$ ($-13°11'38''$).
2. By analyzing the radial density profile, we determined the cluster radius to be 12′.8, equivalent to approximately 10.37 pc (adopting a distance of 2.78 kpc). We found the cluster core and tidal radius to be ∼3′.9 and 20′.

3. Using Gaia data, we have estimated the membership probability and find 1732 most probable cluster members for NGC 2345 with membership probability higher than 70%. The estimated mean proper motion is -1.34 ± 0.20 mas yr^{-1} and 1.35 ± 0.21 mas yr^{-1} in the directions of R.A. and decl., respectively.

4. From the two-color diagram, we have estimated $E(B - V) = 0.63 \pm 0.04$ mag. The combination of 2MASS JHK data and optical data provides $E(J - H) = 0.20 \pm 0.04$ mag and $E(J - K) = 0.34 \pm 0.03$ mag for NGC 2345. We found that the interstellar extinction law is normal toward the cluster region.

5. The distance to NGC 2345 was determined using the Bailer-Jones method and found to be 2.78 ± 0.780 kpc. Additionally, we estimated the distance using the cluster's true distance modulus, resulting in a value of 2.51 ± 0.12 kpc. The age has been determined to be 63 ± 8 Myr through a comparative analysis of the cluster's CMD with $Z = 0.01$ theoretical isochrones provided by Marigo et al. (2017).

6. We have identified the mass function slope to be 1.2 ± 0.08 for all stars located within the complete cluster radius. We found a signature of mass segregation based on slopes in the cluster's core, halo, and overall regions.

7. We found that the dynamical relaxation time for NGC 2345 is larger than the cluster's age. Thus, the dynamical evolution process is ongoing in the cluster; after 100 Myr, it will be dynamically relaxed.

8. We derived the kinematic parameters based on the radial velocity and parallax of the cluster. Utilizing the AD diagram, we determined the apex position to be $(-40°89 \pm 0.12, -44°99 \pm 0.15)$.

9. We studied the effect of Galaxy dynamics on the cluster NGC 2345 by studying its motion in the Galaxy. This shows that the cluster is moving in a circular path and experiencing the same amount of force from the Galactic disk across its journey around the Galactic Center. The cluster has not yet completed a single orbit around the Galactic center.

ORCID iDs

D. Bisht ● https://orcid.org/0000-0002-8988-8434
Geeta Rangwal ● https://orcid.org/0000-0002-6373-770X
Ashish Raj ● https://orcid.org/0000-0001-5981-2255
Arvind K. Dattatrey ● https://orcid.org/0000-0002-4729-9316

References

Allen, C., & Santillan, A. 1991, RMxAA, 22, 255
Allison, R. J., Goodwin, S. P., Parker, R. J., et al. 2009, ApJL, 700, L99
Alonso-Santiago, J., Negueruela, I., Marco, A., et al. 2019, A&A, 631, A124
Astraatmadja, T. L., & Bailer-Jones, C. A. L. 2016, ApJ, 833, 119
Bailer-Jones, C., Rybizki, J., Fouesneau, M., Mantelet, G., & Andrae, R. 2018, AJ, 156, 58
Bailer-Jones, C. A. 2015, PASP, 127, 994
Balaguer-Núñez, L., Tian, K., & Zhao, J. 1998, A&AS, 133, 387
Bastian, N., Covey, K. R., & Meyer, M. R. 2010, ARA&A, 48, 339
Becker, W., & Stock, J. 1954, ZA, 34, 1
Bisht, D., Yadav, R., Ganesh, S., et al. 2019, MNRAS, 482, 1471
Bisht, D., Zhu, Q., Elsanhoury, W., et al. 2022a, AJ, 164, 171
Bisht, D., Zhu, Q., Elsanhoury, W. H., et al. 2021a, PASJ, 73, 677
Bisht, D., Zhu, Q., Yadav, R., Durgapal, A., & Rangwal, G. 2020, MNRAS, 494, 607
Bisht, D., Zhu, Q., Yadav, R., et al. 2021b, AJ, 161, 182
Bisht, D., Zhu, Q., Yadav, R., et al. 2022b, PASP, 134, 044201
Bobylev, V. V., Bajkova, A. T., & Gromov, A. O. 2017, AstL, 43, 241
Caldwell, J. A., Cousins, A., Ahlers, C., Van Wamelen, P., & Maritz, E. 1993, SAAOC, 15, 1
Cantat-Gaudin, T., Anders, F., Castro-Ginard, A., et al. 2020, A&A, 640, A1
Cantat-Gaudin, T., Jordi, C., Vallenari, A., et al. 2018, A&A, 618, A93
Cantat-Gaudin, T., Krone-Martins, A., Sedaghat, N., et al. 2019, A&A, 624, A126
Cardelli, J. A., Clayton, G. C., & Mathis, J. S. 1989, ApJ, 345, 245
Carraro, G., Vázquez, R. A., Costa, E., Ahumada, J. A., & Giorgi, E. E. 2015, AJ, 149, 12
Carraro, G., Villanova, S., Demarque, P., Bidin, C. M., & McSwain, M. 2008, MNRAS, 386, 1625
Carrera, R., Casamiquela, L., Bragaglia, A., et al. 2022, A&A, 663, A148
Castro-Ginard, A., Jordi, C., Luri, X., Cantat-Gaudin, T., & Balaguer-Núñez, L. 2019, A&A, 627, A35
Castro-Ginard, A., Jordi, C., Luri, X., et al. 2018, A&A, 618, A59
Chini, R., Krügel, E., & Kreysa, E. 1990, A&A, 227, L5
Chupina, N., Reva, V., & Vereshchagin, S. 2001, A&A, 371, 115
Chupina, N., Reva, V., & Vereshchagin, S. 2006, A&A, 451, 909
Dias, W. S., Alessi, B. S., Moitinho, A., & Lépine, J. R. D. 2002, A&A, 389, 871
Dias, W. S., Monteiro, H., Lépine, J. R. D., et al. 2018, MNRAS, 481, 3887
Dias, W. S., Monteiro, H., Moitinho, A., et al. 2021, MNRAS, 504, 356
Dib, S., & Basu, S. 2018, A&A, 614, A43
Dib, S., & Henning, T. 2019, A&A, 629, A135
Dib, S., Kim, J., & Shadmehri, M. 2007, MNRAS: Letters, 381, L40
Dib, S., Schmeja, S., & Parker, R. J. 2018, MNRAS, 473, 849
Dib, S., Shadmehri, M., Padoan, P., et al. 2010, MNRAS, 405, 401
Elsanhoury, W., Postnikova, E., Chupina, N., et al. 2018, Ap&SS, 363, 1
Fiorucci, M., & Munari, U. 2003, A&A, 401, 781
Girard, T. M., Grundy, W. M., López, C. E., & van Altena, W. F. 1989, AJ, 98, 227
Groenewegen, M. 2021, A&A, 654, A20
Henden, A., & Munari, U. 2014, CoSka, 43, 518
Holanda, N., Pereira, C. B., Drake, N. A., et al. 2019, MNRAS, 482, 5275
Johnson, D. R. H., & Soderblom, D. R. 1987, AJ, 93, 864
Kalirai, J. S., & Tosi, M. 2004, MNRAS, 351, 649
Kharchenko, N., Piskunov, A., Röser, S., Schilbach, E., & Scholz, R.-D. 2005, A&A, 438, 1163
Kharchenko, N., Piskunov, A., Schilbach, E., Röser, S., & Scholz, R.-D. 2013, A&A, 558, A53
King, I. 1962, AJ, 67, 471
Landolt, A. U. 1992, AJ, 104, 340
Larsen, S. S. 2006, An ISHAPE Users Guide 14
Liu, L., & Pang, X. 2019, ApJS, 245, 32
Luri, X., Brown, A., Sarro, L., et al. 2018, A&A, 616, A9
Marigo, P., Girardi, L., Bressan, A., et al. 2017, ApJ, 835, 77
Maurya, J., Joshi, Y., Elsanhoury, W., & Sharma, S. 2021, AJ, 162, 64
Maurya, J., Joshi, Y., & Gour, A. 2020, MNRAS, 495, 2496

McMillan, S. L., Vesperini, E., & Zwart, S. F. P. 2007, ApJL, 655, L45
Miyamoto, M., & Nagai, R. 1975, PASJ, 27, 533
Moffat, A. 1974, A&AS, 16, 33
Monteiro, H., & Dias, W. 2019, MNRAS, 487, 2385
Pavlík, V., Kroupa, P., & Šubr, L. 2019, A&A, 626, A79
Plunkett, A. L., Fernández-López, M., Arce, H. G., et al. 2018, A&A, 615, A9
Portegies Zwart, S. F., McMillan, S. L., & Gieles, M. 2010, ARA&A, 48, 431
Postnikova, E., Elsanhoury, W., Sariya, D. P., et al. 2020, RAA, 20, 016
Rangwal, G., Yadav, R. K. S., Durgapal, A., Bisht, D., & Nardiello, D. 2019, MNRAS, 490, 1383
Reid, M. J., & Brunthaler, A. 2004, ApJ, 616, 872
Salpeter, E. E. 1955, ApJ, 121, 161
Sariya, D. P., Jiang, G., Sizova, M., et al. 2021, AJ, 161, 101
Schmid-Kaler, T. 1982, New series, Group VI, Vol. 2 (Berlin: Springer-Verlag), 14
Sharma, S., Ghosh, A., Ojha, D., et al. 2020, MNRAS, 498, 2309
Singh, S., Pandey, J. C., & Hoang, T. 2022, MNRAS, 513, 4899

Sneden, C., Gehrz, R., Hackwell, J., York, D., & Snow, T. 1978, ApJ, 223, 168
Spitzer, L., Jr., & Hart, M. H. 1971, ApJ, 166, 483
Stalin, C., Hegde, M., Sahu, D., et al. 2008, BASI, 36, 111
Stetson, P. B. 1987, PASP, 99, 191
Sun, W., de Grijs, R., Deng, L., & Albrow, M. D. 2021, MNRAS, 502, 4350
Tapia, M., Roth, M., Marraco, H., & Ruiz, M. 1988, MNRAS, 232, 661
Tsantaki, M., Delgado-Mena, E., Bossini, D., et al. 2023, A&A, 674, A157
Vallenari, A., Brown, A., Prusti, T., et al. 2023, A&A, 674, A1
Vereshchagin, S., Chupina, N., Sariya, D. P., Yadav, R., & Kumar, B. 2014, NewA, 31, 43
Wilkinson, M. I., & Evans, N. W. 1999, MNRAS, 310, 645
Worrall, D. M., Biemesderfer, C., & Barnes, J. 1992, in ASP Conf. Ser. 25, Astronomical Data Analysis Software and Systems I (San Francisco, CA: ASP), 25
Yadav, R., Sariya, D. P., & Sagar, R. 2013, MNRAS, 430, 3350
Yontan, T. 2023, AJ, 165, 79